Leveraging EAP-Sparsity for Compressed Sensing of MS-HARDI in (k, q)-Space*

Jiaqi Sun, Elham Sakhaee, Alireza Entezari, and Baba C. Vemuri**

CISE Department, University of Florida, Gainesville, FL 32611, USA
vemuri@cise.ufl.edu

Abstract. Compressed Sensing (CS) for the acceleration of MR scans has been widely investigated in the past decade. Lately, considerable progress has been made in achieving similar speed ups in acquiring multi-shell high angular resolution diffusion imaging (MS-HARDI) scans. Existing approaches in this context were primarily concerned with sparse reconstruction of the diffusion MR signal $S(\mathbf{q})$ in the $\mathbf{q}$-space. More recently, methods have been developed to apply the compressed sensing framework to the 6-dimensional joint $(\mathbf{k}, \mathbf{q})$-space, thereby exploiting the redundancy in this 6D space. To guarantee accurate reconstruction from partial MS-HARDI data, the key ingredients of compressed sensing that need to be brought together are: (1) the function to be reconstructed needs to have a sparse representation, and (2) the data for reconstruction ought to be acquired in the dual domain (i.e., incoherent sensing) and (3) the reconstruction process involves a (convex) optimization.

In this paper, we present a novel approach that uses partial Fourier sensing in the 6D space of $(\mathbf{k}, \mathbf{q})$ for the reconstruction of $P(\mathbf{x}, \mathbf{r})$. The distinct feature of our approach is a sparsity model that leverages surfacelets in conjunction with total variation for the joint sparse representation of $P(\mathbf{x}, \mathbf{r})$. Thus, our method stands to benefit from the practical guarantees for accurate reconstruction from partial $(\mathbf{k}, \mathbf{q})$-space data. Further, we demonstrate significant savings in acquisition time over diffusion spectral imaging (DSI) which is commonly used as the benchmark for comparisons in reported literature. To demonstrate the benefits of this approach, we present several synthetic and real data examples.

1 Introduction

Diffusion weighted MRI is a non-invasive way to probe the axonal fiber connectivity in the body by making the MR signal sensitive to water diffusion through tissue. In diffusion weighted MRI, the water diffusion is fully characterized by the diffusion Probability Density Function (PDF) called the ensemble average propagator (EAP) [1]. Under the narrow pulse assumption, the EAP denoted by $P(\mathbf{r})$ and the diffusion signal attenuation $E(\mathbf{q})$ are related through the Fourier

* This research was funded in part by the AFOSR FA9550-12-1-0304 and NSF CCF-1018149 grants to Alireza Entezari and the NIH grant NS066340 to Baba C. Vemuri.
** Corresponding Author.

transform[1]:

$$P(\mathbf{r}) = \int E(\mathbf{q}) \exp(-2\pi j \mathbf{q} \cdot \mathbf{r}) d\mathbf{q} \tag{1}$$

where, $E(\mathbf{q}) = S(\mathbf{q})/S_0$, S_0 is the diffusion signal with zero diffusion gradient, $\mathbf{q}$ is the vector along which the diffusion gradient is applied and $\mathbf{r}$ is the radial vector in the dual space defined through the Fourier relationship above. $P(\mathbf{r})$ at each voxel, captures all the information needed to perform tractography since it is well known that the peaks of this distribution correspond to the local fiber orientations.

In order to estimate the $P(\mathbf{r})$, one normally acquires the diffusion-weighted MR data by sampling $E(\mathbf{q})$ in the $\mathbf{q}$-space along different diffusion sensitizing gradient directions, $\mathbf{q}_k$ (with $1 \leq k \leq N$), spanning a unit hemisphere either over a single shell or multiple shells [2]. For every gradient direction $\mathbf{q}_k$, a full 3-D acquisition in the $\mathbf{k}$-space follows. In order to reconstruct $P(\mathbf{r})$ with a reasonable angular accuracy, a substantial number of sensitizing gradient directions, on multiple shells, are necessary (e.g., $N = 180$). The time incurred in this extensive data acquisition is the key problem making high angular resolution diffusion imaging impractical for clinical use. Very recently however, novel techniques such as multi-band imaging have been implemented, in connection with the well known connectome project, to speed up the acquisition of MS-HARDI [3]. However, these techniques do not exploit the redundancy present in the $(\mathbf{k}, \mathbf{q})$-space which is the main theme of our work in this paper. Thus, the methods presented in this paper maybe applied in addition to the multi-banding techniques to achieve further gains in acquisition time.

Compressed sensing has been applied to magnetic resonance image (MRI) acquisition quite successfully by under sampling in the $\mathbf{k}$-space (frequency space) and still achieving accurate signal reconstruction from this sparse sampling [4]. In the context of diffusion MRI acquisition, there have been some attempts at applying compressed sensing concepts to diffusion spectral imaging (DSI) [5–7]. These techniques reported to use approximately 200 gradient directions to achieve accurate diffusion MR signal reconstruction and this amounts to over forty minutes of scan time which is not practical in many situations such as for movement disorder and Autism patients. As an alternative, there has been some ground breaking work reported in literature on reducing the number of directions along which the magnetic field gradients that are applied to acquire the data in order to achieve sparse reconstruction of the signal and the EAP [8–10]. They however did not apply the compressed sensing jointly to $(\mathbf{k}, \mathbf{q})$-space.

More recently, Mani et al [11] proposed compressed sensing in $(\mathbf{k}, \mathbf{q})$-space by jointly under-sampling $\mathbf{k}$ and $\mathbf{q}$ spaces. This was achieved by under-sampling the $\mathbf{k}$-space randomly for each direction q. Another recent development in the same vein was reported in [12], where joint $(\mathbf{k}, \mathbf{q})$-space compressed sensing is proposed while the sparsity is enforced in the $\mathbf{q}$-space. Naturally their reconstruction is again geared to recovering the $S(\mathbf{k}, \mathbf{q})$ signal, first. To achieve the EAP reconstruction their method employs the typical Fourier transform relationship between $S(\mathbf{k}, \mathbf{q})$ and $P(\mathbf{x}, \mathbf{r})$ post reconstruction of $S(\mathbf{k}, \mathbf{q})$ (using the dual spherical polar Fourier basis) and thus fails to exploit the incoherence between $P(\mathbf{x}, \mathbf{r})$ and $S(\mathbf{k}, \mathbf{q})$.

In this paper, we present a novel technique based on advances in sampling theory to alleviate this time and cost expensive acquisition process that will make MS-HARDI a more viable imaging technique in the clinic. We pose the diffusion-weighted imaging problem as a six-dimensional sampling problem in the 6-dimensional $(\mathbf{k}, \mathbf{q})$-space (i.e., (k_x, k_y, k_z) and (q_x, q_y, q_z)). The diffusion sensitized MR signal and the EAP are related through the 6-dimensional Fourier transform given by,

$$S(\mathbf{k}, \mathbf{q}) = \int_{\mathbb{R}^3} \int_{\mathbb{R}^3} P(\mathbf{x}, \mathbf{r}) \exp(-2\pi j(\mathbf{x}^t \mathbf{k} + \mathbf{q}^t \mathbf{r}))\, d\mathbf{r}\, d\mathbf{x} \qquad (2)$$

For simplicity, we omitted the scaling factor $S(\mathbf{x}, \mathbf{0})$ from the Fourier transform in the equation above.

In order to utilize the compressed sensing principles to achieve accurate reconstruction from partial data, the sparsity constraint is often enforced in the space domain while the sensing occurs in the (dual) frequency space. The notion of incoherent sensing formalizes the idea that sensing basis (e.g., Fourier) and representational basis (e.g., Dirac) are dual to each other; thus yielding full incoherence. Since $(\mathbf{k}, \mathbf{q})$ and $(\mathbf{x}, \mathbf{r})$ spaces are Fourier duals of each other and the acquisition occurs in $(\mathbf{k}, \mathbf{q})$-space, we seek to reconstruct with sparsity constraints in $(\mathbf{x}, \mathbf{r})$-space. The key distinction between our approach and existing approaches is that, enforcing sparsity in $P(\mathbf{x}, \mathbf{r})$ entitles us to leverage incoherent sensing, not only in $\mathbf{k}$, but also in the $\mathbf{q}$-space simultaneously. Therefore, our approach presented here stands to benefit from practical guarantees for accurate reconstruction from partial $(\mathbf{k}, \mathbf{q})$ data. We then combine the $(\mathbf{k}, \mathbf{q})$ sampling with sparse reconstruction to exploit the principle of compressed sensing for reconstruction of $P(\mathbf{x}, \mathbf{r})$. The key ingredient enabling sparse representation for $P(\mathbf{x}, \mathbf{r})$ is accomplished using surfacelet basis. The most attractive feature of surfacelet basis is the inherent directional selectivity that leads to a sparse representation in the $\mathbf{r}$-space. For further details, see Section 2.2.

The rest of the paper is organized as follows, in section 2, we present the theoretical formulation of the sampling and reconstruction problem. Section 3 contains several synthetic and real data experiments demonstrating the performance of our method. Finally, we wrap up in section 4 with conclusions.

2 Formulation

In this section, we present the theoretical formulation for our full 6D Compressed Sensing (CS) and sparse reconstruction of the field of EAPs, $P(\mathbf{x}, \mathbf{r})$.

2.1 Compressed Sensing

The significant achievement of the CS theory [13, 14] is the ability to reconstruct a function from partial data given the function has a sparse representation. The three ingredients of the CS framework necessary to guarantee accurate reconstruction are:

- **Sparsity:** The function to be reconstructed needs to be sparsely representable, possibly in some transform domain.
- **Incoherent Sensing:** The data for reconstruction must be acquired in a domain incoherent (e.g., dual) to the domain in which the function is sparsely representable.
- **Nonlinear Reconstruction:** The reconstruction problem involves an (convex) optimization process.

In the case of diffusion MR imaging, with the presence of the Fourier dual relationship between $(\mathbf{k}, \mathbf{q})$ and $(\mathbf{x}, \mathbf{r})$ space, as illustrated in Equation (2), the above conditions will be met when a proper sparsifying transform is applied to $P(\mathbf{x}, \mathbf{r})$. In this work, we propose to use surfacelets as a choice of sparsifying basis for representation of EAPs.

2.2 The Surfacelet Transform

Measuring the diffusion of water molecules along several directions in HARDI acquisitions is an attempt to capture diffusion anisotropy. It is well known that EAPs capture this local information quite adequately. The key question then is, how best to represent the EAPs that are to be reconstructed from patially sensed data in $(\mathbf{k}, \mathbf{q})$-space? Thus, the primary goal here (in accordance with the principles of CS described above) is to find a basis in which EAPs with their inherent directional information are sparsely representable.

Wavelets, as a common choice of sparsifying transforms, lack directional sensitivity and exhibit inadequacy in efficiently capturing orientational features. As geometric generalizations to wavelets, directional decomposition methods, e.g., ridgelets [15], have been proposed to detect the orientational structures in a signal. Although these transforms can be generalized to higher dimensions, they are only optimal for 2D signals such as images. The three dimensional curvelet (3D-Curvelet) was suggested in [16] for detecting/representing directional information and geometry of the object; however, its high redundancy factor (i.e., ratio of the number of transformed coefficients to the number of signal elements) makes the problem size excessively large, hence, limits its application in diffusion MR image analysis.

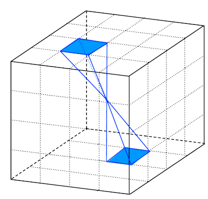

Fig. 1: Frequency partitioning of surfacelet transform

Surfacelets [17], on the other hand, are real three-dimensional transforms and were shown to be particularly efficient for sparse approximation of volumetric data [18]. They have a low redundancy factor (~ 4) and are able to capture directional information which is predominant in the $\mathbf{q}$-space diffusion sensitized MR signal.

The surfacelet transform is implemented as a combination of a multi-scale pyramid with 3D directional filter banks (3D-DFB) [17]. The basis functions are a spatial domain representation of symmetric pyramids partitioning the frequency space. Fig. 1 depicts the support of one surfacelet basis in the frequency domain.

Let Ω denote the rectangular 3-D volume within which we desire to reconstruct the EAPs. Let the total number of voxels in Ω be N_s. In this work, we propose to reconstruct the EAP at each voxel in Ω on a grid within the voxel. In order to fully exploit the power of surfacelet transform, we further restrict this grid to be a cube and denote the length of the side of this cube by N_r. Let P_i ($i = 1, \dots, N_s$) be the EAP at thei^{th} voxel, thus, $P_i \in \mathbb{R}^{N_r \times N_r \times N_r}$. P_i can then be expressed in surfacelet basis $\varphi_m^{(l)}(.)$, corresponding to different scales (l) and spectral directions (m) as:

$$P_i(\mathbf{r}) = \sum_{m,l} c_{m,l} \varphi_m^{(l)}(\mathbf{r}) \tag{3}$$

Let $\mathbf{c}_i := [c_{m,l}]$ be the vector formed by surfacelet coefficients of the i^{th} voxel and denote the surfacelet transform with $\mathcal{S}$. We can then write $\mathbf{c}_i = \mathcal{S}(P_i)$ and seek for a sparse coefficient vector by minimizing ℓ_1 norm of $\mathbf{c}_i$ for each voxel, as described in section 2.3. When we represent the voxel location by $\mathbf{x}$, surfacelet transform of $P(\mathbf{x}, \mathbf{r})$ is essentially $\mathcal{S}(P_i)$ applied on all N_s voxels separately and simultaneously.

The low redundancy factor along with tree-structured (fast) implementation makes the surfacelets practically suitable in dMRI applications, while directional decomposition makes it well-suited for recovering the geometry of EAPs.

2.3 Problem Formulation

Equipped with the sparsifying ability of the surfacelet transform upon EAPs, we are now able to apply the CS theory to achieve direct reconstruction of EAPs from a set of partial samples of $S(\mathbf{k}, \mathbf{q})$. Denote the measured $(\mathbf{k}, \mathbf{q})$-space data over Ω by S and let $\mathscr{F}_u$ be the undersampled 6-D Fourier Transform.We formulate the EAP reconstruction problem as the following optimization problem:

$$\hat{P} = \arg\min_P \left\{ \frac{1}{2} \|\mathscr{F}_u(P) - S\|_F^2 + \mu \sum_{i=1}^{N_s} \|\mathcal{S}(P_i)\|_1 + \gamma \|P\|_{TV_s} \right\} \tag{4}$$

where, μ and γ control the balance between the sparsity regularization and the spatial smoothness regularization. $\mathcal{S}(P_i)$ denotes the coefficients obtained by applying the surfacelet transform to the EAP at the i^{th} voxel in Ω.

In the above objective function, the l_1 norm of the surfacelet coefficients is minimized which promotes sparsity [13, 14] in the surfacelet representation. In addition, we leverage the sparsity of the gradients in the field of EAPs via a total variation (TV) penalty term. The TV norm over the field of EAPs, where each EAP is represented by a volume of size N_s, is denoted by $\| \cdot \|_{TV_s}$ and is defined as follows. First, let us define the total variation of the k^{th} component of an EAP, $k = 1, \dots, {N_r}^3$, over Ω. In this context, we adopt the anisotropic TV norm in our formulation. Represent the k^{th} component of an EAP in the voxel (r, s, t) of Ω by $P^k_{(r,s,t)}$, and represent the 3D volume formed by all of $P^k_{(r,s,t)}$ by P^k. P^k can be regarded as a discrete scalar valued function defined on a 3-D rectangular grid Ω, $P^k : \Omega \rightarrow \mathbb{R}$. Therefore, the anisotropic total variation of P^k can be defined as:

$$TV_{aniso_{3,1}}(P^k) = \sum_{r,s,t} \left\{ \left|P^k_{(r+1,s,t)} - P^k_{(r,s,t)}\right| + \left|P^k_{(r,s+1,t)} - P^k_{(r,s,t)}\right| + \left|P^k_{(r,s,t+1)} - P^k_{(r,s,t)}\right| \right\} \tag{5}$$

Then, the total variation of P over the spatial domain can be defined as follows: $\|P\|_{TV_s} = \left\{ \sum_{k=1}^{N_r^3} \left[TV_{aniso_{3,1}}(P^k)\right]^\alpha \right\}^{\frac{1}{\alpha}}$. In this work, we use $\alpha = 1$.

2.4 Solution using the Split Bregman Algorithm

We solve the optimization problem in Equation (4) by employing the well known Split Bregman method [19]. The problem in Equation (4) can now be reformulated as:

$$\begin{gathered} \hat{P} = \arg\min_P \left\{ \frac{1}{2} \|\mathscr{F}_u(P) - S\|_F^2 + \mu \sum_{i=1}^{N_s} \|\mathbf{c}_i\|_1 + \gamma \|P\|_{TV_s} \right\} \\ s.t.\ P_i = \mathcal{S}^\star(\mathbf{c}_i),\ \ i = 1, \dots, N_s \end{gathered} \tag{6}$$

where, $\mathcal{S}^\star$ denotes the inverse surfacelet transform and P_i is defined as in section 2.3. We can now convert this problem into an unconstrained one by introducing the Lagrange multipliers λ_i:

$$\hat{P} = \arg\min_P \left\{ \frac{1}{2} \|\mathscr{F}_u(P) - S\|_F^2 + \mu \sum_{i=1}^{N_s} \|\mathbf{c}_i\|_1 + \gamma \|P\|_{TV_s} + \sum_{i=1}^{N_s} \frac{\lambda_i}{2} \|P_i - \mathcal{S}^\star(\mathbf{c}_i)\|_F^2 \right\}. \tag{7}$$

In this work we choose to assign $\lambda_1 = \lambda_2 = \cdots = \lambda_{N_s} = \lambda$, then, Equation (7) is simplified to:

$$\hat{P} = \arg\min_P \left\{ \frac{1}{2} \|\mathscr{F}_u(P) - S\|_F^2 + \mu \sum_{i=1}^{N_s} \|\mathbf{c}_i\|_1 + \gamma \|P\|_{TV_s} + \frac{\lambda}{2} \sum_{i=1}^{N_s} \|P_i - \mathcal{S}^\star(\mathbf{c}_i)\|_F^2 \right\}. \tag{8}$$

The Split Bregman algorithm is used to find the optimal solution to the above problem through the following iterations, where t denotes the iteration index:

$$\begin{aligned} (P^{(t+1)}, \mathbf{c}_i^{(t+1)}) = \arg\min_{P, \mathbf{c}_i} & \left\{ \frac{1}{2} \|\mathscr{F}_u(P) - S\|_F^2 + \mu \sum_{i=1}^{N_s} \|\mathbf{c}_i\|_1 + \gamma \|P\|_{TV_s} \right. \\ & \left. + \frac{\lambda}{2} \sum_{i=1}^{N_s} \|P_i - \mathcal{S}^\star(\mathbf{c}_i) - \mathbf{b}_i^{(t)}\|_F^2 \right\} \end{aligned} \tag{9}$$

$$\begin{gathered} \mathbf{b}_i^{(t+1)} = \mathbf{b}_i^{(t)} + (\mathcal{S}^\star(\mathbf{c}_i^{(t+1)}) - P_i^{(t+1)}) \\ \text{for each } i = 1, \dots, N_s \end{gathered} \tag{10}$$

Algorithm:
Split Bregman for EAP reconstruction from partial $(\mathbf{k}, \mathbf{q})$ data

Input: Partial $(\mathbf{k}, \mathbf{q})$-space data S
Output: Reconstructed EAP
Initialization: $P^{(0)} = \mathscr{F}^{-1}(S^0)$
while $\|\mathscr{F}_u(P^{(t)}) - S\|_F^2 < tol$ **do**
  for $n = 1$ **to** N **do**
    $P^{(t+1)} =$
    $\arg\min_P \left\{ \frac{1}{2} \|\mathscr{F}_u(P) - S\|_F^2 + \gamma \|P\|_{TV_s} + \frac{\lambda}{2} \sum_{i=1}^{N_s} \|P_i - \mathcal{S}^\star(\mathbf{c}_i^{(t)}) - \mathbf{b}_i^{(t)}\|_F^2 \right\}$
    for $i = 1$ **to** N_s **do**
      $\mathbf{c}_i^{(t+1)} = \arg\min_{\mathbf{c}_i} \left\{ \mu \|\mathbf{c}_i\|_1 + \frac{\lambda}{2} \|P_i^{(t+1)} - \mathcal{S}^\star(\mathbf{c}_i) - \mathbf{b}_i^{(t)}\|_F^2 \right\}$
    end for
  end for
  for $i = 1$ **to** N_s **do**
    $\mathbf{b}_i^{(t+1)} = \mathbf{b}_i^{(t)} + (\mathcal{S}^\star(\mathbf{c}_i^{(t+1)}) - P_i^{(t+1)})$
  end for
  $t = t + 1$
end while

The minimization in (9) can be performed by iteratively minimizing with respect to P and $\mathbf{c}_i$ separately. The entire algorithm is summarized below.

As illustrated above, we initialize P to be the inverse Fourier Transform of the zero-filled partial data S (by filling the unkown value to be 0), denoted by S^0. The number of inner iterations in the above algorithm N is set to be 1 as suggested in [19].

3 Experimental Results

To demonstrate the performance of our approach, we present experimental results on several synthetic and real datasets in this section.

We use conventional diffusion spectral imaging (DSI) data as the ground truth for comparisons of the reconstruction performance. The $(\mathbf{k}, \mathbf{q})$-space data, acquired for the connectome project, that is composed of 515 diffusion weighted images was considered as fully sampled data. We perform the undersampling of the DSI data with a radial line sampling scheme. It is one of the most widely used schemes for partial Fourier sensing [4], and the theoretical justification for it from a CS perspective was presented in [20].

The undersampling of the entire $(\mathbf{k}, \mathbf{q})$-space is achieved by applying 3-D radial line sampling in $\mathbf{k}$ and $\mathbf{q}$ spaces respectively. We conducted experiments at various rates of undersampling in the joint $(\mathbf{k}, \mathbf{q})$-space. In addition to that, $\mathbf{q}$-space-only and $\mathbf{k}$-space-only undersampling were also performed, respectively, for comparisons.

3.1 Synthetic Data Experiments

We synthesized a fully sampled DSI dataset, $\hat{S}(\mathbf{x}, \mathbf{q})$, over a grid of size $12 \times 12 \times 12$. Each slice consisted of two straight “fiber” bundles crossing each other in the center and a circular “fiber” bundle crossing with the two straight ones at the corners. To fully demonstrate the performance of our method on data sets with complex local geometry, we further increased the complexity of the data set by making the two straight ”fiber” bundles gradually rotate throughout the 12 slices. The diffusion signals were generated using a mixture of Gaussian functions, each being a rotated version of a Gaussian distribution function with zero mean and diagonal covariance matrix $\text{Cov} = \text{diag}\{20, 20, 400\}$. The $(\mathbf{k}, \mathbf{q})$-space data was generated from the $(\mathbf{x}, \mathbf{q})$-space data through a 3-D Fourier Transform (relating $\mathbf{x}$ to $\mathbf{k}$) for each gradient direction $\mathbf{q}$.

We applied conventional DSI reconstruction on the fully sampled synthetic data, to obtain the ground truth field of EAPs. The performance of the reconstruction was quantitatively evaluated by the normalized sum-of-squares error (NSSE) between the reconstructed EAP ($P_{REC}(\mathbf{x}, \mathbf{r})$) and the ground truth EAP ($P_{GT}(\mathbf{x}, \mathbf{r})$), defined as NSSE$=\frac{\sum_{\mathbf{x},\mathbf{r}} \|P_{GT}(\mathbf{x},\mathbf{r}) - P_{REC}(\mathbf{x},\mathbf{r})\|_2^2}{\sum_{\mathbf{x},\mathbf{r}} \|P_{GT}(\mathbf{x},\mathbf{r})\|_2^2}$. We tested our method at various undersampling levels (i.e., partial Fourier sensing rates). At each level, three different undersampling schemes were performed on fully sampled data, namely joint $(\mathbf{k}, \mathbf{q})$-space undersampling, $\mathbf{q}$-space only undersmapling and $\mathbf{k}$-space only undersampling. The reconstruction accuracy for each combination of undersampling level and scheme is computed as the average of 15 repetitions. To demonstrate the advantages of partial sensing in the joint 6-D $(\mathbf{k}, \mathbf{q})$-space compared to partial $\mathbf{k}$ or partial $\mathbf{q}$ sensing, we compared the reconstruction accuracy of these three undersampling schemes at identical sampling rates.

To assess the performance of the proposed method in the presence of noise, we carried out another experiment where various levels of Rician noise was added to the synthetic $(\mathbf{x}, \mathbf{q})$-space data. The noise level is measured by SNR, defined as SNR$=E/\sigma$, E being the mean magnitude of the noise-free signal and σ the standard deviation of the noise. We analyzed the accuracy of reconstruction measured by NSSE, with various undersampling rates and undersampling schemes.

Quantitative results of the reconstruction on partial data (noise-free) with various undersampling rates for different undersampling schemes are presented in Fig. 2(a) and the effects of noise on reconstruction accuracy are shown in Fig. 2(b). As shown in the plots, in both noise-free and noisy case, the proposed compressed sensing in joint $(\mathbf{k}, \mathbf{q})$-space has a better EAP reconstruction accuracy than when undersampling is performed in $\mathbf{k}$-space or $\mathbf{q}$-space only. And with as little as 10-15% of the original data, our method is able to reconstruct the EAPs with very high accuracy even in the presence of noise. As evident from Fig. 2(b), at a moderate level of noise, there is little degradation in the reconstruction accuracy compared to the noise-free case, and at a high level of noise, our method still maintains satisfactory performance. Since NSSE is depicted using a log scale, the reader is cautioned about larger values of NSSE being compressed.

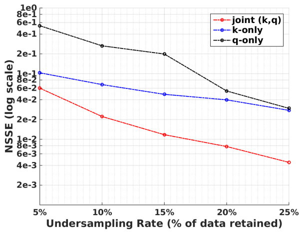

(a) Reconstruction accuracy on noise-free data

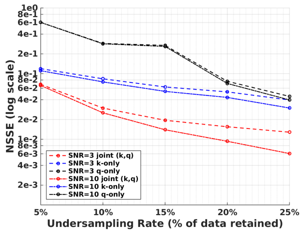

(b) Reconstruction accuracy in presence of various levels of noise

Fig. 2: **Quantitative EAP reconstruction results for synthetic data.**

To further assess the results visually, we plotted the reconstructed EAPs as well as the ground truth EAPs at $\mathbf{r} = 4.5$ for each voxel and showcase selected slices below. In Fig. 3, for slice #12, we show the ground truth EAP field and reconstructed EAP fields with various undersampling schemes from 15% of the full noise-free DSI data. Considering the complexity of the data and the low undersampling rate, our method with joint $(\mathbf{k}, \mathbf{q})$-space undersampling obtained a reconstruction fairly close to the ground truth. While in the **k**-only undersampling case, false crossings appear at voxels with no crossings (as highlighted in green boxes). In the **q**-only case, however, the recovered EAP profiles appear to be of poor quality as depicted in the region marked with a red box. In Fig. 4, we present a visualization of the EAP reconstruction from slice #7 of the noisy data with $SNR = 10$, reconstructed with 15% of the full DSI data. Compared to **k**-only and **q**-only cases, the joint$(\mathbf{k}, \mathbf{q})$-space undersampling yields more accurate reconstructions with respect to the lobe orientations as well as the presence of crossings (representative regions are highlighted in colored boxes).

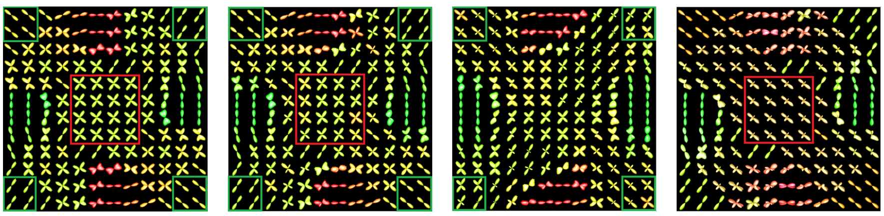

(a) Ground truth (b) $(\mathbf{k}, \mathbf{q}) - joint$ (c) **k**-only (d) **q**-only

Fig. 3: **Visualization of EAP reconstruction for synthetic noise-free data.** Ground truth EAP field and reconstructed EAP fields with different undersampling schemes at a rate of 15% for slice #12 of the noise-free data.

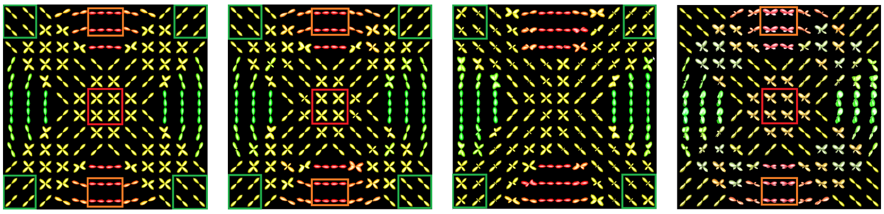

(a) Ground truth (b) $(\mathbf{k}, \mathbf{q}) - joint$ (c) $\mathbf{k}$-only (d) $\mathbf{q}$-only

Fig. 4: **Visualization of EAP reconstruction for noise contaminated synthetic data.** Ground truth EAP field and reconstructed EAP fields with different undersampling schemes at a rate of 15% for slice #7 of the noisy data with SNR=10.

3.2 Real Data Experiments

Real datasets used in the experiments were obtained from the MGH-USC Human Connectome Project(HCP) database (https://ida.loni.usc.edu/login.jsp). We evaluated the proposed method on data acquired using the DSI scheme on a Seimens 3T Connectom scanner, including 514 diffusion weighted images and 1 non-diffusion weighted image. The scan parameters are as follows: maximum b-value $b_{max} = 10,000\, s/mm^2$, TR=5900.0ms, TE=77.0ms, pixel size X=2.0mm, Y=2.0mm and slice thickness 2.0mm, resulting in a $104 \times 104 \times 55$ volume. We picked a $12{\times}12{\times}12$ region from the dataset as our ROI for reconstruction and show the intersection of the ROI with slice #57 from a coronal view in Fig. 5.

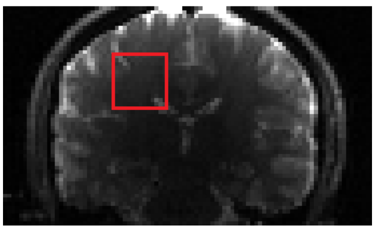

Fig. 5: Coronal view of Slice #57 of the real dataset with ROI presented in the red box.

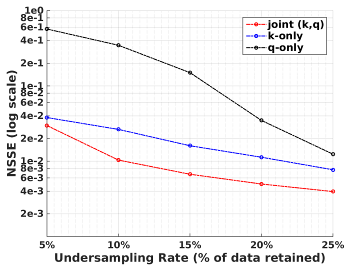

Fig. 6: Quantatitive EAP reconstruction results for real data.

We present the EAP reconstruction accuracy for various undersampling rates in Fig. 6 and visualization of the EAP fields for the coronal slice #57 (slice #11 in ROI) in Fig. 7. From Fig. 6 it is evident that the joint $(\mathbf{k}, \mathbf{q})$-space undersampling leads to higher accuracy in terms of NSSE over the $\mathbf{k}$-only and $\mathbf{q}$-only undersampling. The graph depicts that with 10-15% of the fully sampled data our method yields high fidelity reconstruction of the EAPs. This leads to an acceleration by a factor of 6.7-10 over the standard DSI acquisition. From a comparison of the three reconstructed EAP fields with ground truth in Fig. 7, it is evident that the joint $(\mathbf{k}, \mathbf{q})$-space undersamping method correctly recovered most of the crossings and fiber orientations. However, with $\mathbf{k}$-only undersampling, false crossings and incorrect recovery of EAP lobe orientations are evident in several regions (highlighted in colored boxes). Further, with $\mathbf{q}$-only undersampling, spurious lobes are introduced leading to erroneous orientation information.

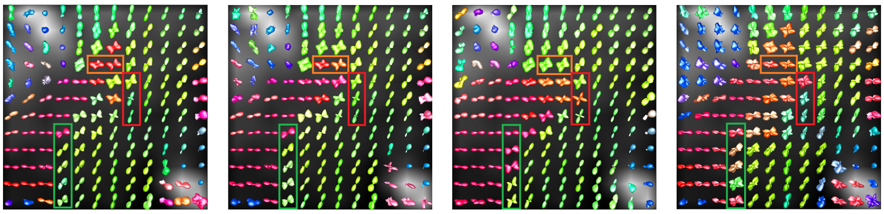

(a) Ground truth (b) $(\mathbf{k}, \mathbf{q}) - joint$ (c) $\mathbf{k}$-only (d) $\mathbf{q}$-only

Fig. 7: **Visualization of EAP reconstruction for real data.** Ground truth EAP field and reconstructed EAP fields with different undersampling schemes at rate 15% for slice #11 in the ROI of real data

In summary, through synthetic and real data experiments we have demonstrated that our method of direct reconstruction of EAPs from CS in joint $(\mathbf{k}, \mathbf{q})$-space yields superior results in comparison to CS applied to either $\mathbf{q}$-space or $\mathbf{k}$-space in isolation.

4 Conclusion

In this paper we presented a novel technique for direct reconstruction of the field of EAPs, $P(\mathbf{x}, \mathbf{r})$, from partial sampling in the 6D joint $(\mathbf{k}, \mathbf{q})$-space. The key distinguishing feature of our method from earlier reported works in literature is that we exploit the principle of Compressed Sensing which states that sensing and reconstruction ought to occur in mutually dual spaces. Consequently, since the data acquisition in diffusion MRI occurs in $(\mathbf{k}, \mathbf{q})$-space, the reconstruction ought to be performed in the $(\mathbf{x}, \mathbf{r})$-space. Moreover, using the Fourier transform relationship between $P(\mathbf{x}, \mathbf{r})$ and $S(\mathbf{k}, \mathbf{q})$, it is natural to exploit the aforementioned duality condition and seek a sparse representation of $P(\mathbf{x}, \mathbf{r})$. We achieved this sparsity through a surfacelet basis which are well known for their directional selectivity in signal/image processing literature. We presented reconstruction results for synthetic and real data demonstrating the performance of our algorithm. Our results show that we can achieve high fidelity of reconstruction of $P(\mathbf{x}, \mathbf{r})$ using just 10-15% of the samples used in a full DSI acquisition. This leads to an acceleration rate of 6.7-10 in acquisition time thus making MS-HARDI a clinically viable diagnostic imaging tool. Our future work will focus on exploring benefits to be acrrued from different sampling schemes in the joint $(\mathbf{k}, \mathbf{q})$-space.

References

1. Callaghan, P.T.: Principles of Nuclear Magnetic Resonance Microscopy. Oxford University Press (1991)
2. Tuch, D.S.: Q-ball imaging. Mag. Res. in Med. (MRM) **52** (2004) 1358–1372
3. Ugurbil, K., Xu, J., *et al*: Pushing spatial and temporal resolution for functional and diffusion MRI in the human connectome project. NeuroImage **80** (2013) 80 – 104 Mapping the Connectome.
4. Lustig, M., Donoho, D., Pauly, J.: Sparse MRI: The application of compressed sensing for rapid MR imaging. Mag. Res. in Med. (MRM) **58** (2007) 1182–1195
5. Landman, B.A., Wan, H., Bogovic, J., van Zijl, P., Bazin, P.L., Prince, J.: Accelerated compressed sensing of diffusion-inferred intra-voxel structure through adaptive refinement. In: ISMRM. (2010)
6. Lee, N., Singh, M.: Compressed sensing based DSI. In: ISMRM. (2010)
7. Menzel, M., Khare, K., King, K.F., Tao, X., Hardy, C.J., Marinelli, L.: Accelerated DSI in the human brain using compressed sensing. In: ISMRM. (2010)
8. Merlet, Sylvain, L., Deriche, R.: Continuous diffusion signal, EAP and ODF estimation via Compressive Sensing in diffusion MRI. Medical Image Analysis **17** (2013) 556–572
9. Merlet, S., Caruyer, E., Deriche, R.: Parametric dictionary learning for modeling EAP and ODF in diffusion MRI. In: MICCAI (3). (2012) 10–17
10. Michailovich, O.V., Rathi, Y., Dolui, S.: Spatially regularized compressed sensing for high angular resolution diffusion imaging. IEEE Trans. Med. Imaging **30** (2011) 1100–1115
11. Mani, M., Jacob, M., Guidon, A., Magnotta, V., Zhong, J.: Acceleration of high angular and spatial resolution diffusion imaging using compressed sensing with multichannel spiral data. Mag. Res. in Med. (MRM) **73** (2015) 126–138
12. Cheng, J., Shen, D., Yap, P.T.: Joint k-q space compressed sensing for accelerated multi-shell acquisition and reconstruction of the diffusion signal and ensemble average propagator. In: ISMRM. (2014) 664
13. Donoho, D.: Compressed sensing. IEEE Trans. on Inf. Theory **52** (2006) 1289–1306
14. Candès, E., Tao, T.: Near-optimal signal recovery from random projections: Universal encoding strategies? IEEE Trans. on Info. Theory **52** (2006)
15. Do, M.N., Vetterli, M.: Image denoising using orthonormal finite ridgelet transform. In: Intl. Symp. on Optical Science and Technology, Intl. Soc. for Optics and Photonics (2000) 831–842
16. Ying, L., Demanet, L., Candes, E.: 3D discrete curvelet transform. In: Optics & Photonics 2005, Intl. Soc. for Optics and Photonics (2005) 591413–591413
17. Lu, Y.M., Do, M.N.: Multidimensional directional filter banks and surfacelets. IEEE Trans. on Image Processing **16** (2007) 918–931
18. Xu, X., Sakhaee, E., Entezari, A.: Volumetric data reduction in a compressed sensing framework. Computer Graphics Forum (CGF), Special Issue on EuroVIS **33** (2014) 111–120
19. Goldstein, T., Osher, S.: The split bregman method for l1-regularized problems. SIAM J. Imaging Sciences **2** (2009) 323–343
20. Willett, R.M.: Smooth sampling trajectories for sparse recovery in MRI. In: Proc. of the 8th IEEE Intl. Symp. on Biomed. Imaging, ISBI 2011, March 30 - April 2, 2011, Chicago, Illinois, USA. (2011) 1044–1047